

Simulations of Astrophysically Relevant Pair Beam Instabilities in a Laboratory Context

Suman Dey* and Günter Sigl†

*II. Institut für Theoretische Physik, Universität Hamburg,
Luruper Chaussee 149, 22761 Hamburg, Germany*

(Dated: January 27, 2025)

The interaction of TeV blazars emitted gamma-rays with the extragalactic background photons gives rise to a relativistic beam of electron-positron (e^-e^+) pairs propagating through the intergalactic medium, producing a cascade through up-scattering low-energy photons. Plasma instability is considered one of the underlying energy-loss processes of the beams. We employ particle-in-cell (PIC) simulations to study the plasma instabilities of ultra-relativistic pair beams propagating in a denser background plasma, using the parameters designed to replicate astrophysical jets under laboratory conditions. In an astrophysical scenario with a broad, dilute beam, electromagnetic instability can be disregarded because its growth rate is slower than that of electrostatic instability, indicating the electromagnetic modes are suppressed. We calculate the physical limit of density contrast at which a warm beam achieves suppression of electromagnetic instabilities in laboratory experiments, consistent with the physically relevant conditions for Blazar-induced beams. We have used a composite Cauchy distribution for the beam particles, which is more realistic in representing the non-Maxwellian nature of pair beams, improving upon previous studies. We investigate the interplay between the magnetic field forming from localized currents and transverse beam momentum spread. We extrapolate to the non-linear feedback of instability where the beam is energetically broadened. We observe that the instability generates a negligible angular broadening for Blazar-Induced beams.

I. INTRODUCTION

Blazars are a type of active galactic nuclei (AGNs) featuring jets of high-energy (i.e. $E \geq 100$ MeV) particles that are oriented almost directly toward Earth. The primary gamma rays with TeV energies travel through the intergalactic medium and interact with the extragalactic background light (EBL). This interaction leads to attenuation of the primary TeV photons, especially for distant blazars. The relativistic e^-e^+ pair plasmas are produced when the TeV gamma-ray interacts with a low-energy EBL photon. The relativistic pairs then undergo inverse Compton (IC) scattering with cosmic microwave background (CMB) photons [1, 2]. This cycle of pair production and IC scattering continues, forming an extended electromagnetic cascade of secondary GeV gamma rays. Nevertheless, there is a disagreement between the expected [3] and observational photon spectra measured from Fermi-LAT and imaging atmospheric (or air) Cherenkov telescopes (e.g., MAGIC, VERITAS, and HESS) [4, 5], known as GeV-TeV tension. One potential explanation for this missing GeV cascade emission can be understood as the deflection of the pairs by the intergalactic magnetic fields (IGMF). This deflection leads to a time delay of the cascade photons. In addition, the deflected particles create extended GeV emission around the blazar, which can extend beyond the field of view of the detector. Consequently, the non-observation of extended GeV emission spectra can be used to estimate

lower bounds on the IGMF strength [4–12]. Furthermore, electromagnetic cascades, influenced by the IGMF, are referred to as "gamma-ray halos" and appear to be bow-tie-shaped structures surrounding point sources in the gamma-ray sky [13], although such phenomena have not yet been observed.

However, alternative hypotheses, including collective plasma effects, can elucidate the phenomenon of cascade emissions. The interaction between the blazar-induced pair beam and the background intergalactic plasma can lead to the growth of plasma instabilities. These instabilities can be either electrostatic or electromagnetic in nature [14]. The collective beam-plasma instabilities can contribute to the energy loss compared to IC cooling. However, the efficiency of the energy loss due to plasma instability is still under debate as the studies by [15–21] only considered the linear evolution to estimate the energy-loss due to instabilities and excluded the non-linear feedback on the beam evolution. [22] conducted a parametric study on the energy-loss length due to plasma instability and the instability power index for the real blazar source 1ES 0229+200. They estimated that the secondary electron pairs lose approximately 1% of their energy over the typical interaction length for IC scattering based on their best-fit scenario. On the other hand, [23] studied the non-linear feedback of electrostatic oblique instability for the same source using a Fokker-Planck equation coupled with the linear wave equation without any contribution of the IGMF. They found that the instability broadens the beam and leads to a minimal energy transfer from the beam to the plasma waves. In this paper, we investigate the instability growth in the linear phase and the feedback of instabilities in the non-linear phase for a non-Maxwellian beam (because of

* suman.dey@desy.de

† guenter.sigl@desy.de

the warm and non-monoenergetic nature of pair-beams generated in blazars) using particle-in-cell (PIC) simulations, improving upon previous studies.

Several approaches have been proposed to mimic this phenomenon in the laboratory, but the primary challenge is the generation of a neutral pair beam. Nevertheless, it is important to emphasize that most traditional beam optics components are not designed to manage beams with both electrons and positrons. Earlier experimental studies at high-intensity laser facilities have reported the ratio of positrons to electrons (N_{e^+}/N_{e^-}), including OMEGA-EP 2014 ($\sim 10\%$) [24], Orion/OMEGA-EP 2015 ($\sim 10\%$) [25], Texas-Petawatt (PW) Laser ($\sim 50\%$) [26], ASTRA-GEMINI Laser system (96%) [27, 28], OMEGA-EP 2021 ($\sim 100\%$) [29], and HiRadMat (97%) [30]. The laboratory experiments provide an excellent opportunity to compare their outcomes with numerical results. Our research contributes to the understanding of how realistically scaled parameters can be selected in order to replicate astrophysical jets within a laboratory setting and also the complete beam evolution for a real astrophysical scenario.

We consider a laboratory-based setup to investigate the evolution of instability with density contrast in the linear and non-linear phases using numerical simulations. For an astrophysical pair beam, [31] established the criteria for setting up a physically relevant simulation:

- i The kinetic energy density ratio of the beam to the background, $\epsilon = \alpha(\langle\gamma\rangle - 1)m_e c^2/k_B T_{bg}$ should be less than unity, where $\langle\gamma\rangle$ is the average bulk Lorentz factor and T_{bg} defines the temperature of the background plasma,
- ii The electrostatic instability growth should dominate over electromagnetic instabilities.

In our study, we fix the first condition and conduct an in-depth investigation into the threshold value of the density contrast that satisfies the second criterion for a broad (or warm) non-Maxwellian beam under laboratory conditions. Subsequently, we extrapolate the non-linear regime from the laboratory to astrophysical scales and examine the effects of non-linear feedback of instability on the angular broadening of beams for a real blazar source. We assume that instability is the dominant mechanism in comparison to the IC cooling for astrophysical pair beams in order to examine the feedback of beam-plasma instability on the pair beam.

The paper is structured as follows: In Section II, we outline the linear growth rates of beam-plasma instabilities, then in Section III, we describe the configuration of a broad (or warm) non-Maxwellian beam distribution function, which is similar to the properties of an astrophysical pair beam. In Section IV, we present the results of the PIC simulation of a beam-plasma system that can be replicated in a laboratory environment. Section V presents the beam divergence and the extrapolation to the non-linear regime, which is interpreted as the feedback of instability. Next, in Section VI, we estimate the

transverse broadening of the beam for 1ES 0229+200-like sources. Finally, Section VII provides the conclusions of our findings.

II. BEAM PLASMA INSTABILITY

Our study focuses on the unstable dynamics of an ultra-relativistic neutral beam composed of electrons and positrons following the same momentum distribution. The beam propagates in a neutral background plasma consisting of electrons with no bulk velocity and immobile protons without having an external magnetic field. The system is characterized using two key parameters: the bulk Lorentz factor γ of the pair beam and the density ratio $\alpha = n_{b0}/n_{bg}$ representing the peak beam density (n_{b0}) relative to the background plasma density (n_{bg}). Given our focus on the behavior of ultra-relativistic dilute beams, we can reasonably consider that $\alpha \ll 1$ and $\gamma \gg 1$. The current filamentation instability (Cfi) is an electromagnetic instability characterized by the excitation of both electric and magnetic field modes, with the unstable modes oriented perpendicular to the beam momentum. In contrast, the oblique instability (Obl) represents an electrostatic mode in which the unstable modes are oriented obliquely to the beam momentum. Using the definition of plasma frequency, $\omega_p = (4\pi n_{bg} e^2/m_e c^2)^{1/2}$, the maximum theoretical linear growth rates of the dominant modes for an ultra-relativistic ($v_b \sim c$) beam can be described as follows [32],

$$\delta_{\text{Cfi,theory}} = \left(\frac{\alpha}{\gamma}\right)^{1/2} \omega_p, \quad (1)$$

$$\delta_{\text{Obl,theory}} = \frac{\sqrt{3}}{2^{4/3}} \left(\frac{\alpha}{\gamma}\right)^{1/3} \omega_p. \quad (2)$$

We investigate the dominant growth rates of these instabilities for a warm non-Maxwellian beam, considering a set of physical parameters relevant to laboratory conditions and likely extrapolate to model the astrophysical scenario.

III. REALISTIC PAIR BEAM DISTRIBUTION FUNCTION

Previous studies [19, 31, 33, 34] on astrophysical plasma scenarios, specifically, collision-less space plasmas, are focused on Maxwellian non-monoenergetic beams having small energy spread. This does not accurately represent real scenarios due to the highly non-monochromatic and broad nature of astrophysical pair distributions. Although Maxwellian beams are straightforward to generate in simulations, a more effective approach would involve superimposing two or more relativistic Cauchy (Breit-Wigner) distribution beams to better replicate relatively broad (or warm) non-Maxwellian beams [30]. To compare the plasma properties in these two cases, we employ the concept of plasma screening

length, or Debye screening, which refers to the ability of a plasma to shield or screen out electric fields over short distances. We evaluate the plasma screening length (λ_{scr}) for both Maxwellian and Cauchy distribution functions by applying the limit for the static field ($\omega/k \rightarrow 0$) of the dielectric tensor. Thus, the longitudinal component of the dielectric tensor reaches a finite value. As the screening length is applicable primarily at large distances, we use the long-wavelength limit, setting $k \rightarrow 0$. Given that the axisymmetry, $\mathbf{k} = (k_{\parallel}, 0, k_{\perp})$ can be assumed for a neutral pair beam without affecting generality. Under this assumption, the dielectric tensor component parallel to the beam propagation direction can be expressed as follows [14, 32, 35, 36],

$$\varepsilon_l = 1 + \sum_s \frac{m_s \omega_{p,s}^2}{k^2} \int \frac{\mathbf{k} \cdot \nabla_{\mathbf{p}} f_s(p)}{\omega - \mathbf{k} \cdot \mathbf{v}} d^3 \mathbf{p}, \quad (3)$$

where p denotes the normalized momentum, f_s represents the normalized distribution function, $\omega_{p,s} = (4\pi n_s q_s^2 / m_s c^2)^{1/2}$ is the plasma frequency, and n_s defines the number density for each species s . The plasma screening length can be evaluated as [37, 38],

$$\begin{aligned} \lambda_{\text{scr}}^{-2} &= \lim_{k \rightarrow 0} \left\{ \lim_{\omega/k \rightarrow 0} k^2 (\varepsilon_l - 1) \right\} \\ &= -4\pi \sum_s \frac{\omega_{p,s}^2}{c^2} \int_0^{\infty} \gamma p \frac{\partial f_s(p)}{\partial p} dp, \end{aligned} \quad (4)$$

For a relativistic scenario, a simplistic normalized Maxwellian beam can be described as follows,

$$f_s(p) = \frac{1}{4\pi\sigma_{\parallel,0} K_2(1/\sigma_{\parallel,0})} \exp\left(-\frac{p}{\sigma_{\parallel,0}}\right), \quad (5)$$

where $K_2(1/\sigma_{\parallel,0})$ is the modified Bessel function of the second kind. Since the pair beam distribution functions are non-thermal, we define $\sigma_{\parallel,0}$ as the initial longitudinal momentum spread. In astrophysical jets, beam particles have an enhanced high-energy tail compared to a Maxwellian distribution. Considering a simple case, the normalized suprathermal beam distribution can be written as follows,

$$f_s(p) = \frac{1}{\pi^2} \left(1 + \frac{p^2}{\sigma_{\parallel,0}^2}\right)^{-2}, \quad (6)$$

Therefore, the plasma screening length for the Maxwellian beam described by equation (5) is calculated as $\lambda_{\text{scr}} \simeq \sigma_{\parallel,0}^{1/2} c \cdot \omega_{p,s}^{-1}$. For the suprathermal Cauchy beam described by equation (6), the expression becomes $\lambda_{\text{scr}} \simeq 0.88 \sigma_{\parallel,0}^{1/2} c \cdot \omega_{p,s}^{-1}$. The plasma screening lengths for Maxwellian and Cauchy distributions are approximately the same, which means that in both cases, the fundamental behavior is similar, differing only at the high-energy tail. To better capture this, we investigate the evolution

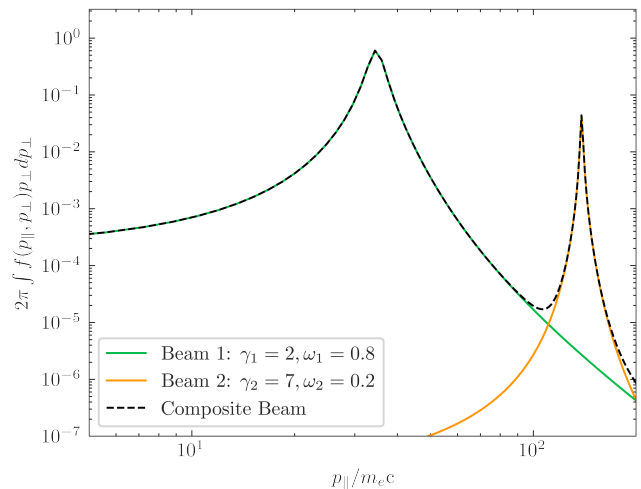


FIG. 1. The distribution function described by equation (7) for a composite broad beam with $\langle \gamma \rangle = 3$ and $\alpha = 10^{-3}$ is used in PIC simulations. The green line corresponds to sub-beam 1 with $\gamma_1 = 2$ and weight factor, $\omega_1 = 0.8$. Orange line represents the sub-beam 2 with $\gamma_2 = 7$ and weight factor, $\omega_2 = 0.2$. The initial longitudinal momentum spread, $\sigma_{\parallel,0} = 1.0$ MeV, the initial transverse momentum spread, $\sigma_{\perp,0} = 0.5$ MeV, and a mean longitudinal momentum, $\mu_{1,2} = 0.511(\gamma_{1,2}^2 - 1)^{1/2}$ MeV for each sub-beams. The black dashed line is the composite non-Maxwellian beam.

of an ultra-relativistic beam with a realistic composite Cauchy distribution in our simulation,

$$\begin{aligned} f(\mathbf{p}; \mu, \sigma_{\parallel,\perp}) &\propto \omega_1 \left[1 + \gamma_1^2 \frac{(p_x - \mu_1)^2}{2\sigma_{\parallel,0}^2} + \gamma_1^2 \frac{p_y^2 + p_z^2}{2\sigma_{\perp,0}^2} \right]^{-2} \\ &+ \omega_2 \left[1 + \gamma_2^2 \frac{(p_x - \mu_2)^2}{2\sigma_{\parallel,0}^2} + \gamma_2^2 \frac{p_y^2 + p_z^2}{2\sigma_{\perp,0}^2} \right]^{-2}, \end{aligned} \quad (7)$$

In the present work, we use a system of "plasma units" where the fundamental constants, $\omega_p = c = k_B = 1$. In this study, the distribution function of electron-positron (e^+e^-) pairs produced is non-thermal. To replicate an astrophysical pair beam in the laboratory, we must account for it producing electron-positron pairs with an opening angle of approximately $\theta_0 \sim \gamma^{-1}$. Considering a longitudinally warm or broad and transversely kinematically cold beam, the initial transverse momentum spread can be scaled as,

$$\sigma_{\perp,0} = p \sin(\theta_0) = \gamma m_e \sin(\gamma^{-1}) \sim m_e. \quad (8)$$

This suggests that the highly relativistic particle will exhibit a wide range of longitudinal momenta, and a transverse momentum spread approximately equal to the electron mass. This configuration closely resembles the characteristics of an astrophysical pair beam.

Figure 1 shows the pair beam distribution following equation (7), integrated across the transverse momen-

tum. The following distribution function perfectly resembles the non-Maxwellian nature of the beam at high energies.

IV. PIC SIMULATIONS

A. Simulation set up

In order to model the propagation of a warm beam through a background plasma in a two-dimensional Cartesian configuration, we employ EPOCH-2D PIC simulation code [39]. In the initial condition setup, the length of simulation box of the longitudinal direction is defined by $L_{\parallel,box} = 120c \cdot \omega_p^{-1}$ and the transversal direction is represented by $L_{\perp,box} = 120c \cdot \omega_p^{-1}$. We use four types of particles: beam electrons and beam positrons exhibiting relatively broad Cauchy momentum distribution, background plasma consisting of electrons with no bulk velocity, and background protons, which are immobile due to their larger mass. The initial beam density profile is given by $n_b = n_{b0}[1 + (y/R_{y,0})^2]^{-2}$ where $R_{y,0} = 110c \cdot \omega_p^{-1}$ denotes the initial rms beam transverse spatial width, the initial peak beam density $n_{b0} = \alpha n_{bg}$, and the background particles have a density of $n_{bg} = 10^{16} \text{ cm}^{-3}$ for different values of α in the simulations. In our series of simulations, we explore α values of 0.0005, 0.005, and 0.05 while maintaining a fixed effective Lorentz factor, $\langle \gamma \rangle = 3$ for all cases. Although these α values are significantly higher than those relevant to real TeV Blazars, the chosen range within the laboratory regime provides ample scope for reliable extrapolation to lower values. We employ periodic boundary conditions in the longitudinal direction and open boundary conditions in the transverse direction to simulate a finite-width beam. Periodic boundary conditions ensure that fields and particles arriving at one side of the simulation box reappear at the opposite side, but for the open boundary system, particles simply transmit through the boundary and leave the system. Simulations are conducted up to the total time $4500\omega_p^{-1}$ to capture the linear, the non-linear growth phase, and the saturation region. The criteria for a physically relevant configuration of the beam-plasma system is that the kinetic energy density ratio must satisfy the condition $\epsilon < 1$. We select beam Lorentz factors of $\gamma_1 = 2$ for sub-beam 1 and $\gamma_2 = 7$ for sub-beam 2. The corresponding relative weight factors are $\omega_1 = 0.8$ for sub-beam 1 and $\omega_2 = 0.2$ for sub-beam 2. In accordance with the previous section, the warm neutral pair beam is characterized by maintaining an initial longitudinal momentum spread, $\sigma_{\parallel,0} = 1.0 \text{ MeV}$ with a mean longitudinal momentum, $\mu_{1,2} = 0.511(\gamma_{1,2}^2 - 1)^{1/2} \text{ MeV}$ and an initial transverse momentum spread, $\sigma_{\perp,0} = 0.5 \text{ MeV}$ for each sub-beams. This indicates that in the background plasma rest frame, the composite beam is initially transversely cold and longitudinally warm as the initial angular spread, $\Delta\theta_0 \equiv \sigma_{\perp,0}/\sigma_{\parallel,0} = 0.5$, which is less than 1. A comprehensive overview of the simulation param-

TABLE I. The summary of the PIC Simulation configuration for the simulation run.

Parameters	Value
Number of Dimensions	2 (x beam dir., y trans.)
Boundary conditions along x	periodic
Boundary conditions along y	open
$L_{x,box}(L_{\parallel,box})$	$120 c \cdot \omega_p^{-1}$
$L_{y,box}(L_{\perp,box})$	$120 c \cdot \omega_p^{-1}$
N_x	880
N_y	880
N_p (for every species)	200
N_{tot} (for every species)	1.5488×10^8
Timestep Δt	0.95 CFL-Criterion
Maxwell Solver	Yee (Second-order scheme)
Order of the FDS ^a	6
Particle Pusher	Higuera & Cray
Particle Shape Function	Third Order B-Spline
Current Filtering	5-fold (1-2-3-4 steps)
n_{bg}	10^{16} cm^{-3}
T_{bg}	$\alpha(\langle \gamma \rangle - 1)600 \text{ keV}$
Background particles	Electrons & immobile Protons
Beam particles	Electrons & Positrons
Distribution Function	equation (7)
ϵ	0.85
Total time T	$4500 \omega_p^{-1}$

^a Finite difference scheme

TABLE II. The overview of the sub-beam parameters for the Cauchy beam distribution function.

Parameters	Sub-beam 1	Sub-beam 2
$\gamma_{1,2}$	2	7
$\omega_{1,2}$	0.8	0.2
$\mu_{1,2}$ (MeV)	$0.511(\gamma_1^2 - 1)^{1/2}$	$0.511(\gamma_2^2 - 1)^{1/2}$
$\sigma_{\parallel,0}$ (MeV) (alias $\Delta p_{x,0}$)	1.0	1.0
$\sigma_{\perp,0}$ (MeV) (alias $\Delta p_{y,0}$)	0.5	0.5

eters is presented in Table I, and Table II outlines the sub-beam parameters.

B. Growth of plasma instabilities and evolution of fields

The primary numerical measurable quantity that we can access in a simulation run is the growth of the fields. The initial noise due to the thermal fluctuation of the background plasma can influence the evolution of the fields. The initial noise of the system is inversely proportional to ϵ , i.e., Initial noise $\propto 1/(N_{tot}\epsilon)$, where N_{tot} is the total number of simulation particles [40]. Increasing the background plasma temperature results in a decrease of the parameter ϵ . Therefore, we increase N_{tot} to offset the significant noise caused by high background plasma temperatures. Throughout these simulations, we maintain a very low initial noise level. We employ a Yee Maxwell field solver with 6th-order field interpola-

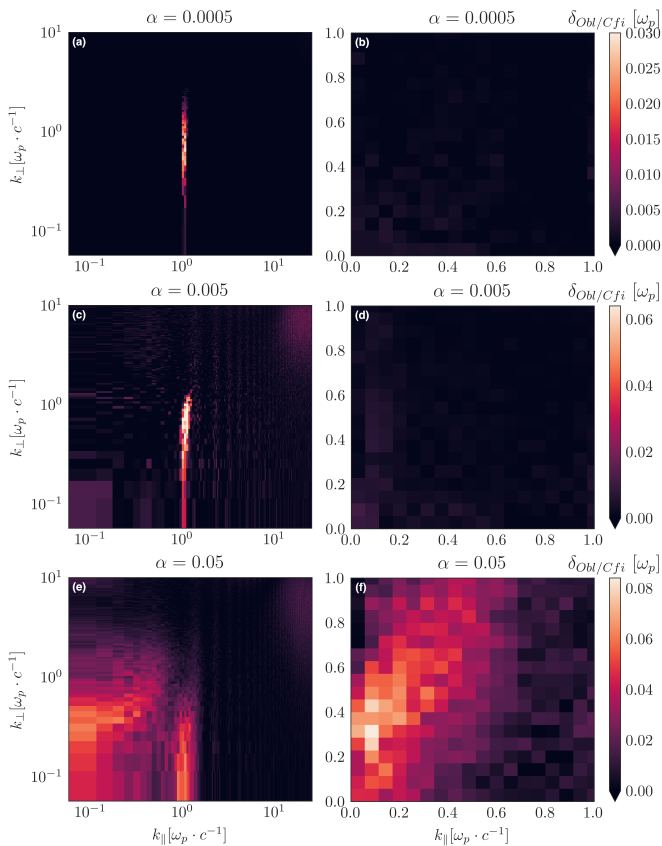


FIG. 2. Two-dimensional snapshots of the spectral growth rate of electrostatic instability are obtained using the Fourier spectrum of $\mathbf{E} \parallel \mathbf{k}$ modes for $\alpha = 0.0005$ at $t\omega_p \sim 670$, $\alpha = 0.005$ at $t\omega_p \sim 310$, and $\alpha = 0.05$ at $t\omega_p \sim 170$ (figures (a), (c), and (e) along the **left** column). The spectral growth rates of the current filamentation instability are determined from the Fourier spectrum of the transverse component of the magnetic field for $\alpha = 0.0005$ at $t\omega_p \sim 610$, $\alpha = 0.005$ at $t\omega_p \sim 310$, and $\alpha = 0.05$ at $t\omega_p \sim 133$ (figures (b), (d), and (f) along the **right** column). With increasing α , the electrostatic mode remains unresolved, and the electromagnetic mode becomes dominant.

tion and a 3rd-order B-spline shape function (yielding a 5th-order weighting) for placing particles on the grid. The default multiplying factor for this field solver is set to 0.95 of the Courant–Friedrichs–Lewy (CFL) criterion on time steps. A particle pusher is implemented following the method described by [41]. To reduce numerical noise, we apply a 5-fold current smoothing, following the approach outlined by [42]. The wave number is expressed as having a component parallel to the direction of propagation of the beam, denoted as $k_{\parallel} = k_x$ and the component perpendicular to the beam propagation is given by $k_{\perp} = (k_y^2 + k_z^2)^{1/2}$. In figures 2a, 2c, and 2e, we present the growth rates for the oblique instability plotted against wavevectors for different α values with beam parameters specified in Table II. The resonant electrostatic mode, which is the fastest growing mode, is observed around $k_{\parallel} \sim c \cdot \omega_p^{-1}$. The figures 2b, figures 2d,

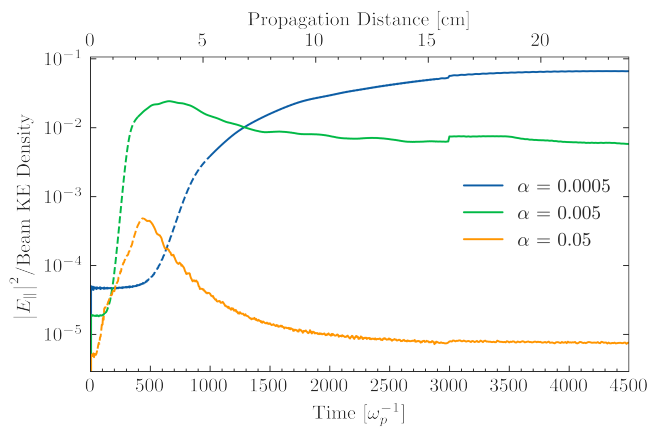


FIG. 3. The fraction of beam kinetic energy converted into the longitudinal electric field across all modes is shown with respect to time on the bottom x-axis and beam propagation distance on the top x-axis. The beam parameters outlined in Table II are applied in every simulation for different density contrast α . The dashed lines represent the linear growth rate for each α , with lower values of α leading to a greater dominance of the electric field modes.

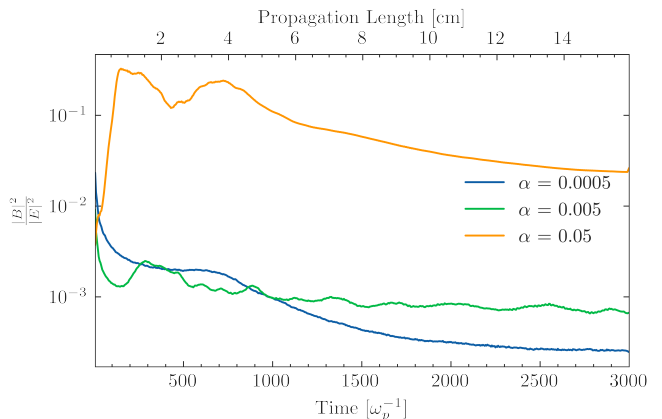


FIG. 4. The comparison of magnetic field to electric field strength across all modes is shown as a function of time (bottom x-axis) and beam propagation distance (top x-axis). The beam parameters specified in Table II are used for all simulations with varying density contrast α , similar to Figure 3. As α decreases, the magnetic field strength becomes significantly weaker than the electric field strength, with $|B|^2 \ll |E|^2$.

and 2f indicate that electromagnetic modes are relatively more important as α increases, which becomes significant for $\alpha = 0.05$. The maximal filamentation growth is observed around $k_{\parallel} \sim 0$. The transition between the dominant current filamentation modes to oblique modes is immediately observed while decreasing α from 0.05 to 0.005. Figure 3 illustrates the time evolution of the longitudinal electric fields for different values of α . As α increases, a significantly smaller fraction of the beam kinetic energy is converted into longitudinal electric fields, indicating that the oblique mode faints as the beam be-

comes relatively denser. Figure 4 shows that as α decreases, the magnetic field strength becomes significantly smaller than that of the electric field, i.e., $|B| \ll |E|$. Analytically, if we solve the full dispersion relation of the beam for the electrostatic resonant eigenmode, we can find the relationship between the magnetic and electric field strength as $|B| \sim 2\delta_{Obl}|E|/\omega_p$ [43]. Consequently, for ultra-relativistic dilute beams (i.e., $\alpha \ll 1$), the condition of growth rate, $\delta \ll 1$ is satisfied for the electrostatic modes. For instance, when $\alpha = 0.005$ and effective Lorentz factor $\langle \gamma \rangle = 3$, the theoretical electrostatic growth rate is calculated as $\delta_{Obl,theo} \sim 0.071\omega_p$. The maximum electrostatic growth rate measured in the simulation is approximately around $\delta_{Obl,sim} \sim 0.064\omega_p$. This fulfills the consistency of the simulation with the analytical results.

C. Interplay between magnetic field and beam momentum

When a neutral pair beam propagates through a plasma, small perturbations can arise, leading to the spatial separation of electrons and positrons in the beam, resulting in the formation of localized currents. The separation can be on the scale of the skin depth of the beam. The localized currents can create filaments, leading to the generation of magnetic fields. Figure 5 shows the fraction of beam kinetic energy converted into the magnetic field for different α values. For increasing values of α , the magnetic field strength increases because the electron and positron filaments start to separate spatially, producing self-generated localized currents [27]. The electromagnetic instability grows until the wavelength of unstable modes is comparable to the Larmor radius of the particles in the self-generated magnetic field, causing them to become trapped in the magnetic fields [44, 45]. Consequently, an electromagnetic counterpart emerges despite the overall beam remaining neutral. Accordingly, at higher density contrast, magnetic fields are generated and the filamentation instability develops because of the transverse magnetic pressure linked to the filaments, causing the total magnetic field to predominantly align in the transverse direction ($|B| \sim |B_\perp|$). However, after the linear growth phase, there is a secular growth of filamentation instability before saturation (which starts at $t \sim 510\omega_p^{-1}$, as shown in figure 5), particularly for $\alpha = 0.05$. This is due to the formation of a small cavity, which is more clearly observed in the spatial structure of the magnetic field in a 3D simulation [46, 47]. As the magnetic pressure within these unscreened cavities causes them to expand, more current is exposed, leading to secular growth. The secondary growth will eventually saturate as the net current in the cavity decreases. Figure 6 depicts the evolution of the spatial structure of the transverse magnetic field at the initial state and during the primary linear growth phase. As α increases, the filamentation instability gives rise to the development

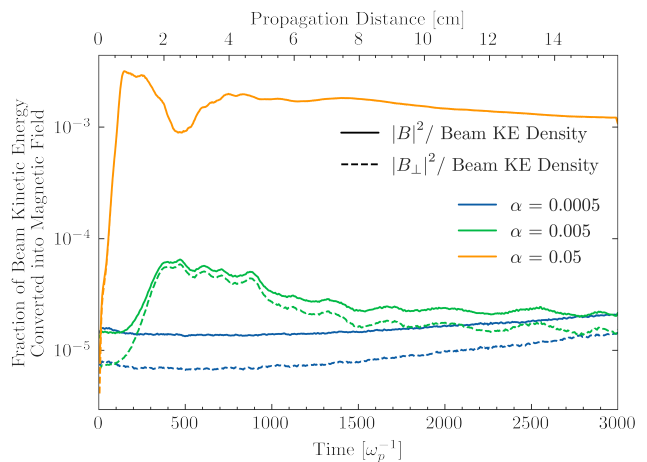


FIG. 5. The fraction of beam kinetic energy transferred into the magnetic field across all modes is shown with respect to time (bottom x-axis) and the distance the beam travels during this time (top x-axis). For every simulation with varying density contrast α , the beam parameters provided in Table II are applied similarly as figure 3 and 4. The solid lines represent the total magnetic field, and the dashed lines depict only the transverse component of the magnetic field.

of distinct transverse magnetic filament structures. The phenomenon of generation of current filamentation has been studied explicitly using both analytical and semi-analytical methods by [19, 48–53]. Figure 7 illustrates the fraction of beam kinetic energy transferred to the transverse magnetic field for different initial transverse beam momentum spreads. As the initial transverse beam momentum increases, with $\sigma_{\parallel,0} = 1.0$ MeV fixed, the induced transverse magnetic field decreases, suggesting a decrease in transverse current filamentation instability in the linear growth regime. However, while a warm beam can drive current filamentation instability during the linear growth phase, it also enhances the conditions for secondary filamentation growth in the non-linear regime. Figure 8 shows the two-dimensional momentum distribution at different simulation timestamps for various values of α . Due to the different growth rates associated with varying α values, the linear growth phase begins and ends at different times. At the start of the linear growth phase, the beam is focused, maintaining its stability without significant perturbations affecting the longitudinal beam momentum (p_{\parallel}) and the transverse beam momentum (p_{\perp}). As the instability growth progresses, the beam spreads energetically both in the transverse and longitudinal direction, resulting in an overall broadening of its distribution. The transversal broadening in the non-linear phase is reduced as the beam gets diluted because the electromagnetic modes become suppressed. As previously explained, in the filamentation-instability-driven scenario, a secondary filamentation instability develops during the nonlinear phase. This leads to a non-linear feedback that significantly causes strong transverse momentum broadening.

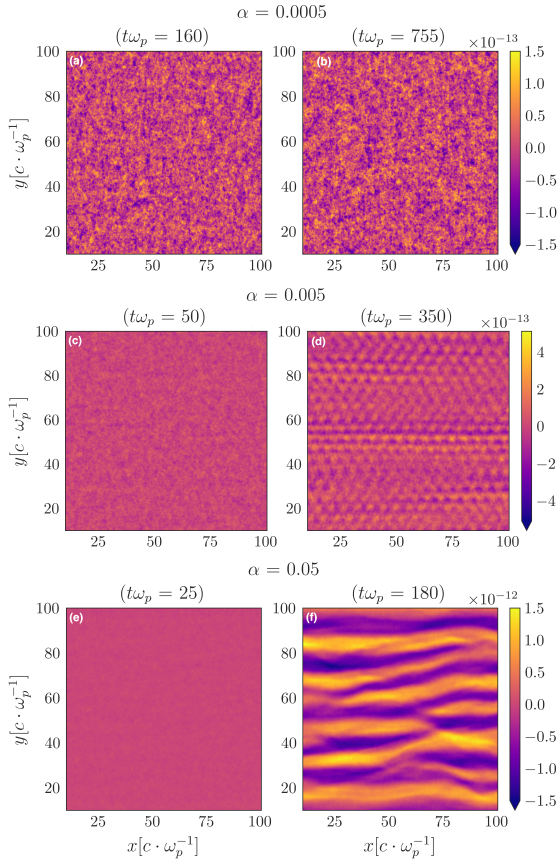


FIG. 6. The evolution of the transverse magnetic field with varying density contrast α . The color scale represents the fraction of beam kinetic energy converted into each mode of the associated transverse magnetic field, i.e., $(B_{\perp})_k / \sqrt{\text{Beam KE Density}}$. The figures (a), (c), and (e) along the **left** column illustrate the state before the linear growth phase of the instability sets in, whereas figures (b), (d), and (f) along the **right** column show the evolution of the transverse magnetic field at the instability growth phase.

V. BEAM DIVERGENCE

To study the effect of beam transverse divergence resulting from instabilities, we have to consider the non-linear regime, where the beam is influenced by the instability feedback and has already passed the linear growth phase. Additionally, our simulation does not include an external magnetic field. Thus, in the absence of any focusing force, the envelope equation for the beam can be expressed as follows [54–56]:

$$\frac{d^2 R_y}{dt^2} - \frac{\epsilon_n^2}{4 \langle \gamma \rangle^2 R_y^3} = 0, \quad (9)$$

where $\langle \gamma \rangle = \sum_i \omega_i \gamma_i$ represents the effective Lorentz factor, ϵ_n is the normalized emittance, and $R_y = \langle r^2 \rangle^{1/2}$

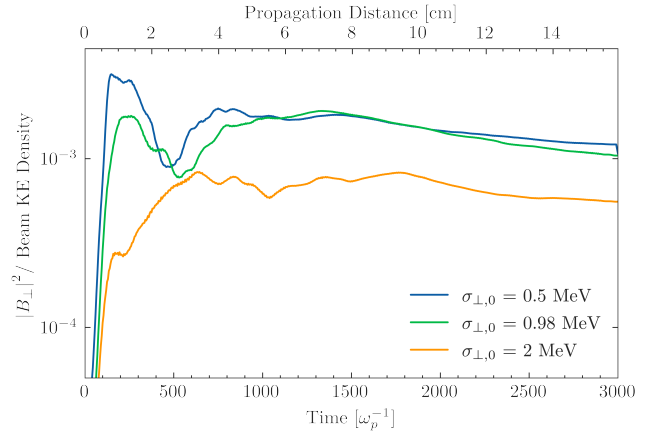


FIG. 7. The fraction of beam kinetic energy transferred into the transverse magnetic field across all modes with respect to time is represented on the bottom x-axis, and the propagation distance is shown on the top x-axis. In every simulation, the density contrast is fixed at $\alpha = 0.05$ and $\sigma_{\parallel,0} = 1.0$ MeV, while the initial transverse momentum of the composite beam is varied. The beam parameters listed in Table II are used. As the initial transverse momentum increases or the beam becomes colder, both the current filamentation instability and the secondary growth are diminished.

is the normalized root-mean-square (rms) beam spatial width at a given time. However, it is important to note that we have used an open boundary along the transverse direction with a beam initial spatial width of $R_{y,0}$ in our simulation, which indicates that the beam has a finite waist, as shown in the schematic figure 9. The correlation between r and dr/dt (alias p_{\perp}) is negligible (uncorrelated due to the minimal divergence nature at the waist). This means the correlation term, defined as $\langle r \times (dr/dt) \rangle$ would be zero, considering the cylindrical coordinate system. Because of the barycentric origin of transverse phase space, the average transverse momentum $\langle dr/dt \rangle$ also vanishes (see appendix A1). Since the normalized emittance has no correlation term [54, 57], we can express the normalized beam emittance as,

$$\begin{aligned} \epsilon_n &\simeq \frac{\langle \gamma \rangle}{2} \left(\langle r^2 \rangle \times \left\langle \left(\frac{dr}{dt} \right)^2 \right\rangle \right)^{1/2}, \\ &= \frac{1}{2m_e} R_y \Delta p_{\perp}, \end{aligned} \quad (10)$$

where Δp_{\perp} is the transverse beam momentum spread at a given time. The detailed calculation of normalized beam emittance is presented in appendix A1. The normalized beam emittance corresponds to the area of the transverse phase space. Using equation (9) and the fact that the normalized emittance is conserved, we can further express the beam spatial width as,

$$R_y(t) \equiv R_y = R_{y,0}^4 \left\{ 1 + \frac{\epsilon_n^2}{2 \langle \gamma \rangle^2 R_{y,0}^4} (t - t_0)^2 \right\}^{1/4}, \quad (11)$$

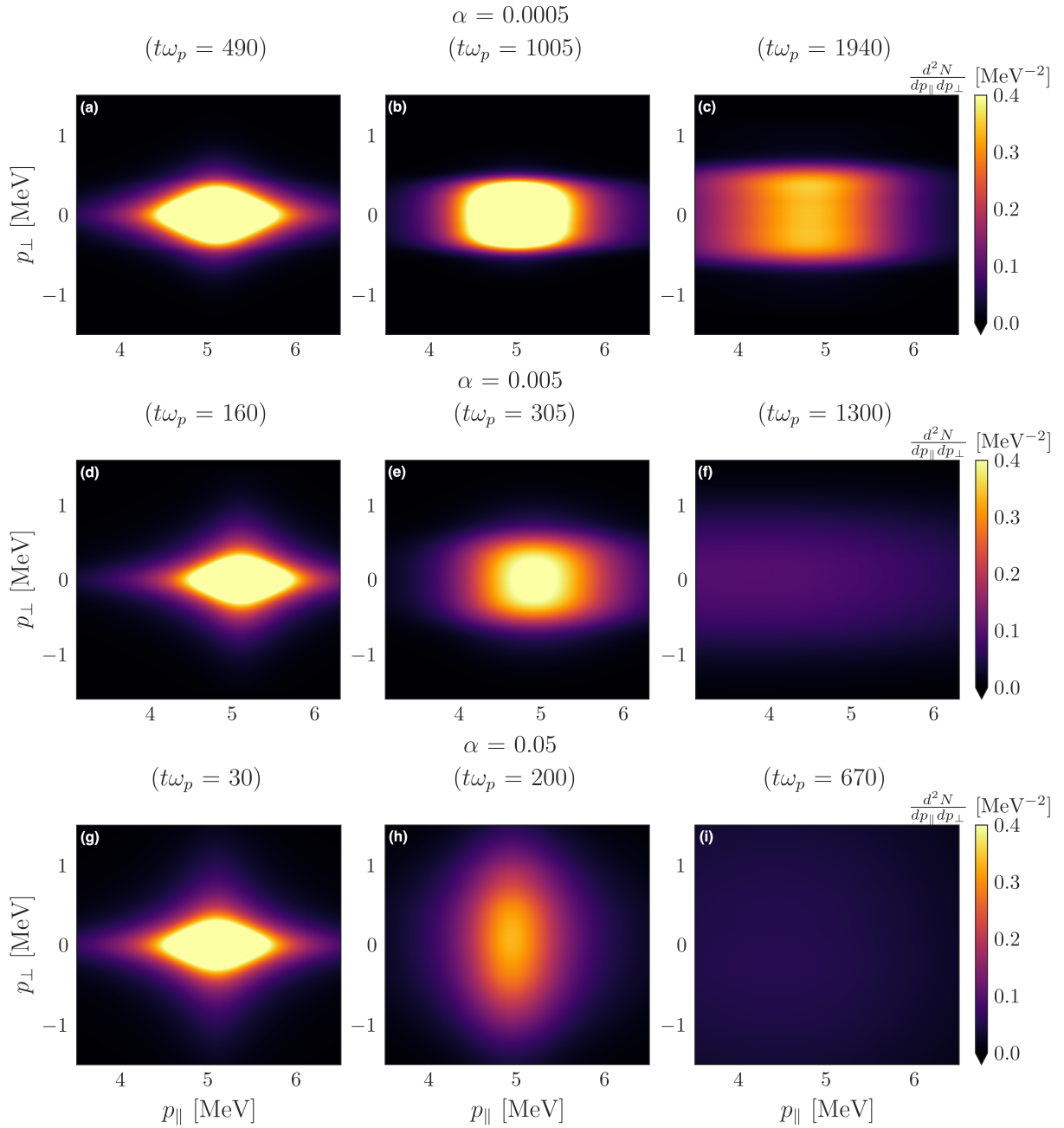


FIG. 8. Momentum distribution in two dimensions for different stages of instability growth for different values of α . The figures (a), (d), and (g) on the **left row**: before starting the linear growth, figures (b), (e), and (h) on the **middle row**: during the linear growth phase, and figures (c), (f), and (i) on the **right row**: at the end of the non-linear regime (starts to saturate). The color scale represents the beam distribution function in momentum space and has a unit of MeV^{-2} . The different timestamps for instability growths depend on the dominant instability modes according to Table III.

The rate at which the beam broadens can be analytically computed using equation (11) as follows,

$$\tau_{\text{brod}}^{-1} = \frac{1}{R_y} \frac{dR_y}{dt} = \frac{\epsilon_n^2}{8 \langle \gamma \rangle^2 R_{y,0}^2} (t - t_0) \times \left\{ 1 + \frac{\epsilon_n^2}{2 \langle \gamma \rangle^2 R_{y,0}^4} (t - t_0)^2 \right\}^{-1/2} \quad (12)$$

The right side of the equation (12) depends on the normalized beam emittance, initial rms beam spatial width, transverse momentum, and growth time. We can quantitatively estimate the transverse beam broadening rate (τ_{brod}^{-1}) at the non-linear regime caused by the feedback of instability. Table III summarizes the dominant instabilities that are responsible for momentum broadening in the non-linear phase across the range of α values con-

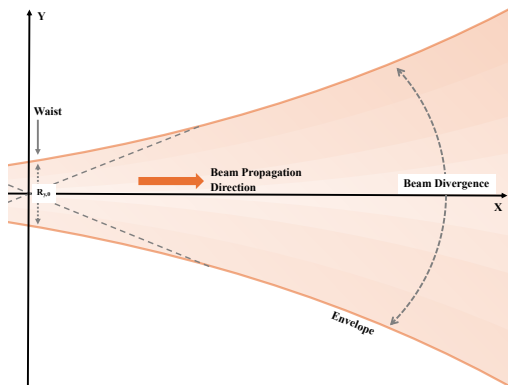


FIG. 9. A schematic representation of the spatial structure of the beam, showing the increase in rms beam spatial width as the distance from the beam waist increases.

TABLE III. Summary of the dominant instabilities in the linear growth phase that are responsible for momentum broadening in non-linear regions for different α runs.

$\Delta\theta_0$ [rad]	$\langle\gamma\rangle$	α	Dominant instability
0.5	3	0.0005	Oblique
		0.005	Oblique
		0.05	Transverse current filamentation

sidered in our simulation. The beam with $\alpha = 0.005$ is the threshold on a laboratory scale where the non-linear feedback of electrostatic instability is observed, leading to the energetic broadening of the beam over time.

A. Extrapolation to the non-linear regime

Here we establish a power-law scaling relationship between the angular broadening ($\Delta\theta_{\text{non-lin}}$) due to non-linear instability feedback and α , with the other parameters fixed as specified in Table II. The power-law scaling is estimated at the times when the beam has already formed its shape and enters into the saturation region. Figure 10 illustrates the scaling of the $\Delta\theta_{\text{non-lin}}$ ($\equiv \Delta p_{\perp}/\Delta p_{\parallel}$) with α and the errorbars have been estimated with a deviation of $\Delta(t\omega_p) = \pm 10$, is shown in the inset plot. Table IV represents the data used to obtain the linear plot. The power-law scaling can be expressed as,

$$\left(\frac{\Delta\theta_{\text{non-lin}}}{1 \text{ rad}}\right) \sim 0.75 \cdot \alpha^{0.19}, \quad (13)$$

The dependence of $\Delta\theta_{\text{non-lin}}$ on α is relatively weak.

VI. IMPLICATIONS FOR 1ES 0229+200-LIKE SOURCES

The total isotropic-equivalent luminosity (\mathcal{L}) of Blazar and photon energies influence the density of electron-positron pairs. The upper limit of the pair density can

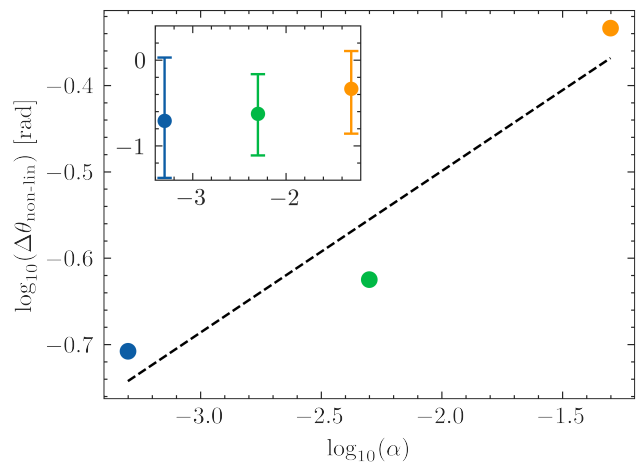


FIG. 10. The power-law scaling of $\Delta\theta_{\text{non-lin}}$ approximately at the end of non-linear phase with α is observed at $t\omega_p \simeq \{1940, 1300, 670\}$ respectively for $\alpha = \{0.0005, 0.005, 0.05\}$. This indicates the moment when the beam starts to enter the saturation phase. The black dashed line represents the fitted line. The embedded plot displays the error bars associated with the main plot (also shown in Table IV), with the errors calculated for $\Delta(t\omega_p) = \pm 10$.

TABLE IV. The overview of the Δp_{\perp} data for different α values and the fitting parameters are obtained from the simulation. The errors are estimated for $\Delta(t\omega_p) = \pm 10$.

$\langle\gamma\rangle$	$\log_{10}(\Delta\theta_0)$ [rad]	$t\omega_p$	α	$\log_{10}(\Delta\theta_{\text{non-lin}})$ [rad]
3	-0.3	1940	0.0005	$-0.708^{+0.03}_{-1.37}$
		1300	0.005	$-0.625^{+0.16}_{-1.11}$
		670	0.05	$-0.334^{+0.11}_{-0.86}$

be derived assuming a balance between pair production and the IC cooling mechanism [15] as,

$$n_b \simeq 1.9 \cdot 10^{-21} \text{cm}^{-3} \left(\frac{1+z}{2}\right)^{3\zeta-4} \left(\frac{\mathcal{L}}{10^{45} \text{erg/s}}\right) \left(\frac{\gamma}{10^7}\right), \quad (14)$$

The parameter $\zeta = 4.5$ for $z < 1$ can be derived from the local star formation rate analysis [58]. As a benchmark scenario, we consider the blazar source 1ES 0229+200 located approximately at $z \approx 0.14$, fixing other parameters $n_{\text{IGM}} = 10^{-7} \text{cm}^{-3}$ and the fiducial value of $\mathcal{L} = 10^{45} \text{erg/s}$, consistent with [21]. The density ratio can be expressed as:

$$\alpha \simeq 9.1 \cdot 10^{-17} \left(\frac{\gamma}{10^7}\right), \quad (15)$$

The intrinsic opening angle of the pair beam with a Lorentz boost 10^7 is determined by $\Delta\theta_0 \sim 10^{-7}$ rad. The angular spread at the non-linear stage can be expressed from our extrapolation as,

$$\Delta\theta_{\text{non-lin}} = \left.\frac{\Delta p_{\perp}}{\Delta p_{\parallel}}\right|_{\text{non-lin}} \sim 6.7 \cdot 10^{-4} \left(\frac{\gamma}{10^7}\right)^{0.19} \text{ rad}, \quad (16)$$

The resulting angular spread due to the instability feedback for a beam with a Lorentz boost 10^7 is nearly $6.7 \cdot 10^{-4}$ rad, which leads to a negligible angular broadening of the pair beam, considering the fact that the IC cooling rate is slower than the instability growth.

VII. CONCLUSIONS

We revisit the evolution of blazar-induced neutral pair beams under laboratory conditions using PIC simulations. The aim of our study is to estimate the maximal density contrast for which the beam can be considered dilute in the sense that electromagnetic instabilities are subdominant, and in this parameter regime, the laboratory experiments can mimic the astrophysical case. The conclusions of this study can be summarized as follows:

- In the absence of an external magnetic field, the dominant instability depends on the peak beam density. For a warm beam, at significantly higher beam density contrast (~ 0.05), the beam is more likely to produce localized currents, which can lead to transverse current filamentation during the linear growth phase. A highly warm beam can drive the current filamentation instability during the linear growth phase, it simultaneously enhances the chances of secondary filamentation growth in the non-linear regime, eventually leading to saturation.
- Our results suggest that in laboratory experiments, a longitudinally broad (or warm) beam with an initial angular spread, $\Delta\theta_0 = 0.5$ and $\alpha \leq 0.005$ can be classified as a "dilute beam", achieving a regime where electromagnetic instabilities are suppressed, and the oblique instability dominates (as specified in Table III). In the non-linear regime, the feedback of instability leads to a transverse broadening of the beam. Thus, $\alpha \leq 0.005$ represents the physical limit for observing these effects in laboratory conditions.
- Using the beam envelope method and the concept of beam emittance on propagation, we have estimated the transverse beam broadening rate in the non-linear regime for different α values. We obtain a power-law scaling relationship for the transverse beam broadening rate with α , which can henceforth be derived using equation (12) approximately,

$$\left(\frac{\tau_{\text{brod}}^{-1}}{1 \text{ sec}^{-1}} \right) \propto \alpha^{0.19}, \quad (17)$$

- In a very dilute beam, electromagnetic instabilities are subdominant, allowing electrostatic oblique instabilities to take precedence. This leads to a decrease of the emerging magnetic field strength, suggesting that the rates of transverse beam broadening are also reduced. In astrophysical scenarios, the background intergalactic medium (IGM)

has a density of approximately $n_{\text{IGM}} \sim 10^{-7} \text{ cm}^{-3}$, which translates to the density contrast of $\alpha = 10^{-21} - 10^{-15}$ for lower redshift ($z < 1$) TeV sources. This indicates that the beam is very dilute, suggesting that the non-linear feedback from instability effects is almost marginal, leading to a negligible transverse broadening. The instability has a minimal impact on cascade production for TeV blazars.

- While preparing this paper, another study by [59] was published that conducted a quantitative assessment of the blazar 1ES 0229+200 using an alternative numerical approach to investigate the angular spread of the beam induced by the instability. The study concluded that the angular broadening is very minimal. In a steady-state scenario, the angular spread of the beam is approximately $5 \cdot 10^{-6}$ rad for a Lorentz factor of 10^7 , with a gamma-ray photon mean-free path of about 13 kpc. However, for the same source, we note that our extrapolated estimation of the angular broadening of a beam with bulk Lorentz factor of 10^7 in the non-linear phase (approaching saturation regime) is $\sim 6.7 \cdot 10^{-4}$ rad, which is about two orders of magnitude larger than what was estimated in [59].

In conclusion, we have identified the physical upper limit of the beam density contrast for which a warm beam can be inferred as "dilute," conducting real-life laboratory experiments that mimic the realistic astrophysical pair beam produced from TeV blazars. Although we have studied the evolution of pair beams in an unmagnetized background plasma, it is also worthwhile to explore their behavior in a magnetized plasma, as this can suppress instability growth and modify the condition for dilute beams. Another important consideration can be collisional effects, particularly if the collisional frequency becomes comparable to the growth rate of the filamentation instability, which can further suppress the instability.

ACKNOWLEDGMENTS

SD was funded by the Deutsche Forschungsgemeinschaft (DFG, German Research Foundation) under Germany's Excellence Strategy– EXC 2121 "Quantum Universe"– 390833306. This project was conceived by GS. The authors gratefully acknowledge the EPOCH code development team. The authors acknowledge the HPC facility of the Maxwell computational resources operated at Deutsches Elektronen-Synchrotron (DESY), Hamburg, Germany. The authors would like to thank Prof. Martin Pohl and Dr. Mahmoud Alawashra for the interesting discussions during the Zeuthen visit.

Appendix A: Normalized beam emittance

From the definition, the normalized beam emittance in cylindrical coordinates can be represented as,

$$\epsilon_n = \frac{\langle \gamma \rangle}{2} \left\{ \langle r^2 \rangle \times \left\langle \left(\frac{dr}{dt} \right)^2 \right\rangle - \left\langle \left(r \cdot \frac{dr}{dt} \right) \right\rangle^2 \right\}^{1/2}, \quad (\text{A1})$$

The transverse rms energy spread can be expressed as,

$$\Delta p_{\perp} = \left\{ \left\langle \left(\frac{dr}{dt} \right)^2 \right\rangle - \left\langle \frac{dr}{dt} \right\rangle^2 \right\}^{1/2}, \quad (\text{A2})$$

According to the statistical definition of emittance, the origin is positioned at the barycenter of the phase space, indicating that the beam is centered and symmetric around this point [60]. As a result, $\langle dr/dt \rangle = 0$, which further translates

$$\Delta p_{\perp} \simeq \left\langle \left(\frac{dr}{dt} \right)^2 \right\rangle^{1/2}, \quad (\text{A3})$$

Given that r and dr/dt are uncorrelated, the second term $\langle r \cdot (dr/dt) \rangle^2$ in equation (A1) also vanishes. Consequently, ϵ_n can be described as the area encompassed by the beam transverse phase space,

$$\epsilon_n \simeq \frac{1}{2m_e} R_y \Delta p_{\perp}, \quad (\text{A4})$$

Appendix B: Energy Budget

We have studied a quantitative estimation of the proportion of total energy of the system allocated to beam kinetic energy, total field energy, and the energy of background particles. For instance, based on the parameters listed in Table II, figure 11 indicates that initially, around 45.8% of the total energy is allocated to the kinetic energy of the beam, while approximately 54.2% is distributed to the energy of the background particles. This reflects the initial condition of our simulation setup, where the ratio of the beam to background kinetic energy density is $\epsilon \sim 0.85$. The growth of plasma instabilities can facilitate energy transfer from the beam to the background. The energy transfer takes place after the instability growth phase ends. However, our observations indicate that this is inefficient, resulting in only a minor increase in the energy of background particles.

Appendix C: A composite Maxwell-Jüttner distribution

In this section, we draw a comparison between a non-monochromatic or broad beam with a composite Cauchy distribution and a Maxwellian beam distribution in terms

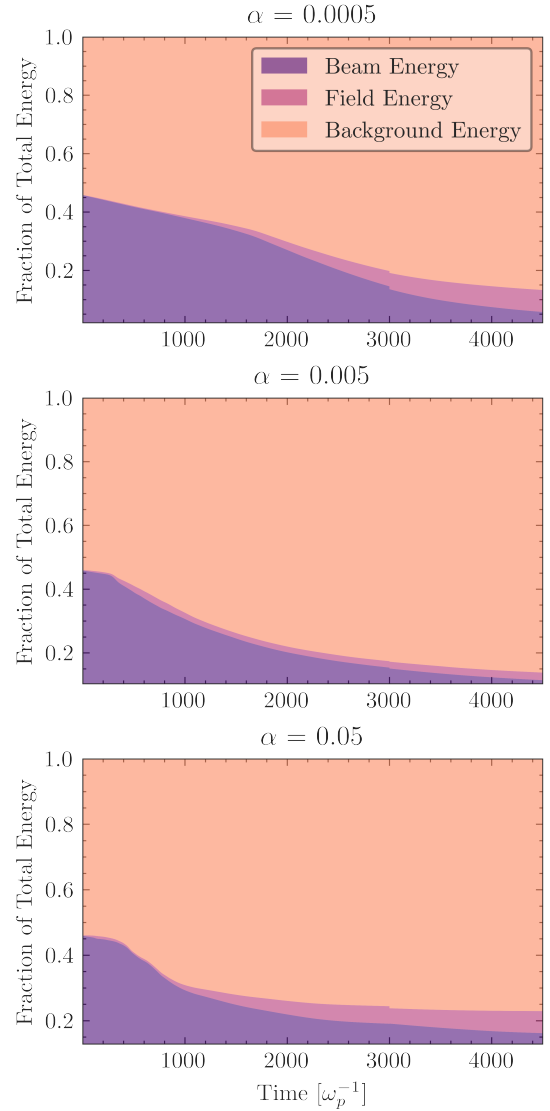


FIG. 11. The allocation of the total energy of the system between the beam kinetic energy, the total electromagnetic field energy, and the energy of the background medium is presented over time with different density contrast α . Each simulation run uses beam parameters as detailed in Table II.

of instability growth. The alternative method to construct a non-monoenergetic non-Maxwellian beam can be described by composing two (or more) Maxwellian sub-beams expressed in the following way [20]:

$$f(\mathbf{p}; \mu, \sigma_{\parallel, \perp}) \propto \omega_1 e^{-\gamma_1 \left[\left\{ 1 + \frac{(p_x - \mu_1)^2}{2\sigma_{\parallel, 0}^2} + \frac{p_y^2 + p_z^2}{2\sigma_{\perp, 0}^2} \right\}^{1/2} \right]} + \omega_2 e^{-\gamma_2 \left[\left\{ 1 + \frac{(p_x - \mu_2)^2}{2\sigma_{\parallel, 0}^2} + \frac{p_y^2 + p_z^2}{2\sigma_{\perp, 0}^2} \right\}^{1/2} \right]}. \quad (\text{C1})$$

where $\gamma_{1,2}, \mu_{1,2}$ values are same as used before for Cauchy distribution. A comprehensive overview of the parameters for this type of beam distribution is provided in

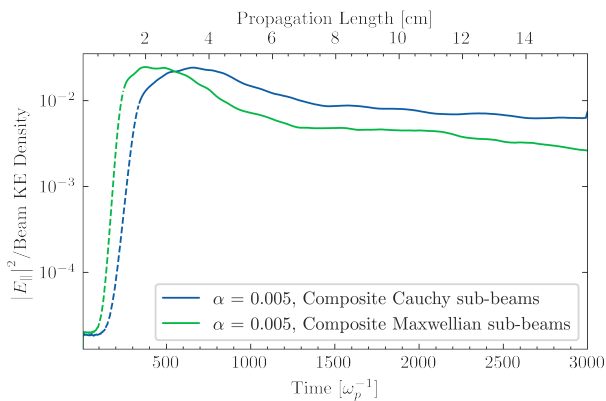


FIG. 12. The time evolution of the fraction of initial beam kinetic energy is converted into the electric field for a broad (or non-monochromatic) beam distribution of composite Maxwellian sub-beams and composite Cauchy sub-beams, for $\alpha = 0.005$. The dashed lines represent the linear growth phase, while the cross marks denote the beginning and end of instability growth.

the same manner as for the Cauchy beam distribution, as shown in Table II. Figure 12 shows the fraction of beam kinetic energy converted into the electric field for composite Maxwellian sub-beams from equation (C1) in comparison to the composite Cauchy distribution from equation (7). The distance or time over which the instability develops generally does not depend on the beam distribution; however, the impact of non-linear behavior for these two cases causes changes in the saturation level by factors of a few.

-
- [1] R. J. Gould and G. P. Schröder, *Phys. Rev.* **155**, 1408 (1967).
- [2] G. R. Blumenthal and R. J. Gould, *Rev. Mod. Phys.* **42**, 237 (1970).
- [3] F. A. Aharonian, in *27th International Cosmic Ray Conference* (2001) arXiv:astro-ph/0112314.
- [4] A. Neronov and D. V. Semikoz, *Phys. Rev. D* **80**, 123012 (2009), arXiv:0910.1920 [astro-ph.CO].
- [5] A. Neronov and I. Vovk, *Science* **328**, 73 (2010).
- [6] A. Elyiv, A. Neronov, and D. V. Semikoz, *Phys. Rev. D* **80**, 023010 (2009), arXiv:0903.3649 [astro-ph.CO].
- [7] A. M. Taylor, I. Vovk, and A. Neronov, *Astron. Astrophys.* **529**, A144 (2011), arXiv:1101.0932 [astro-ph.HE].
- [8] K. Takahashi, M. Mori, K. Ichiki, and S. Inoue, *Astrophys. J. Lett.* **744**, L7 (2012), arXiv:1103.3835 [astro-ph.CO].
- [9] I. Vovk, A. M. Taylor, D. Semikoz, and A. Neronov, *Astrophys. J. Lett.* **747**, L14 (2012), arXiv:1112.2534 [astro-ph.CO].
- [10] R. Durrer and A. Neronov, *Astron. Astrophys. Rev.* **21**, 1 (2013).
- [11] V. A. Acciari, I. Agudo, T. Aniello, S. Ansoldi, L. Antonelli, A. A. Engels, M. Artero, K. Asano, D. Baack, A. Babić, *et al.*, *Astron. Astrophys.* **670**, A145 (2023).
- [12] F. Aharonian, J. Aschersleben, M. Backes, V. B. Martins, R. Batzofin, Y. Becherini, D. Berge, B. Bi, M. Bouyahiaoui, M. Breuhaus, *et al.*, *Astrophys. J. Lett.* **950**, L16 (2023).
- [13] A. E. Broderick, P. Tiede, M. Shalaby, C. Pfrommer, E. Puchwein, P. Chang, and A. Lamberts, *Astrophys. J.* **832**, 109 (2016), arXiv:1609.00387 [astro-ph.HE].
- [14] A. Bret, M.-C. Firpo, and C. Deutsch, *Phys. Rev. E* **72**, 016403 (2005).
- [15] A. E. Broderick, P. Chang, and C. Pfrommer, *Astrophys. J.* **752**, 22 (2012), arXiv:1106.5494 [astro-ph.CO].
- [16] F. Miniati and A. Elyiv, *Astrophys. J.* **770**, 54 (2013), arXiv:1208.1761 [astro-ph.CO].
- [17] R. Schlickeiser, D. Ibscher, and M. Supsar, *Astrophys. J.* **758**, 102 (2012).
- [18] R. Schlickeiser, S. Krakau, and M. Supsar, *Astrophys. J.* **777**, 49 (2013).
- [19] L. Sironi and D. Giannios, *Astrophys. J.* **787**, 49 (2014), arXiv:1312.4538 [astro-ph.HE].
- [20] S. Vafin, I. Raffighi, M. Pohl, and J. Niemiec, *Astrophys. J.* **857**, 43 (2018).
- [21] R. Alves Batista, A. Saveliev, and E. M. de Gouveia Dal Pino, *Mon. Not. Roy. Astron. Soc.* **489**, 3836 (2019), arXiv:1904.13345 [astro-ph.HE].
- [22] L. E. E. Castro, S. Rossoni, and G. Sigl, (2024), arXiv:2405.15390 [astro-ph.HE].
- [23] M. Alawashra and M. Pohl, *Astrophys. J.* **964**, 82 (2024), arXiv:2402.03127 [astro-ph.HE].
- [24] H. Chen, G. Fiksel, D. Barnak, P.-Y. Chang, R. Heeter, A. Link, and D. Meyerhofer, *Phys. Plasmas* **21**, 10.1063/1.4873711 (2014).
- [25] H. Chen, F. Fiuza, A. Link, A. Hazi, M. Hill, D. Hoarty, S. James, S. Kerr, D. Meyerhofer, J. Myatt, *et al.*, *Phys. Rev. Lett.* **114**, 215001 (2015).
- [26] E. Liang, T. Clarke, A. Henderson, W. Fu, W. Lo, D. Taylor, P. Chaguine, S. Zhou, Y. Hua, X. Cen, *et al.*, *Sci. Rep.* **5**, 13968 (2015).
- [27] G. Sarri, K. Poder, J. Cole, W. Schumaker, A. Di Piazza, B. Reville, T. Dzelzainis, D. Doria, L. Gizzi, G. Grittani, *et al.*, *Nat. Commun.* **6**, 6747 (2015).
- [28] C. Hooker, J. Collier, O. Chekhlov, R. Clarke, E. Divall, K. Ertel, B. Fell, P. Foster, S. Hancock, A. Langley, *et al.*, in *J. Phys. IV (Proceedings)*, Vol. 133 (EDP sciences, 2006) pp. 673–677.
- [29] J. Peebles, G. Fiksel, M. Edwards, J. von der Linden, L. Willingale, D. Mastro Simone, and H. Chen, *Phys. Plasmas* **28**, 10.1063/5.0053557 (2021).
- [30] C. D. Arrowsmith *et al.*, *Nature Commun.* **15**, 5029 (2024), arXiv:2312.05244 [physics.plasm-ph].

- [31] I. Rafighi, S. Vafin, M. Pohl, and J. Niemiec, *Astron. Astrophys.* **607**, A112 (2017).
- [32] A. Bret, L. Gremillet, and M. E. Dieckmann, *Phys. Plasmas* **17**, 10.1063/1.3514586 (2010).
- [33] M. Beck, O. Ghosh, F. Grüner, M. Pohl, C. B. Schroeder, G. Sigl, R. D. Stark, and B. Zeitler, (2023), arXiv:2306.16839 [astro-ph.HE].
- [34] A. Kempf, P. Kilian, and F. Spanier, *Astron. Astrophys.* **585**, A132 (2016).
- [35] A. Bret, L. Gremillet, and D. Benisti, *Phys. Rev. E* **81**, 036402 (2010).
- [36] O. Ghosh, *In Light and Dark: Laboratory and Astrophysical Probes of the Late Universe*, Ph.D. thesis, Staats- und Universitätsbibliothek Hamburg Carl von Ossietzky (2022).
- [37] E. M. Lifshitz, Landau and Lifshitz course of theoretical physics **10**, Sec (1981).
- [38] V. Silin, *Sov. Phys. JETP* **11**, 1136 (1960).
- [39] C. P. Ridgers *et al.*, *Plasma Phys. Control. Fusion* **57**, 113001 (2015).
- [40] M. Beck, *Numerical Studies for a Laboratory Astrophysics Experiment of Unstable Electron-Positron Beams*, Ph.D. thesis, Staats- und Universitätsbibliothek Hamburg Carl von Ossietzky (2023).
- [41] A. V. Higuera and J. R. Cary, *Phys. Plasmas* **24**, 10.1063/1.4979989 (2017).
- [42] J.-L. Vay and B. B. Godfrey, *Comptes Rendus Mécanique* **342**, 610 (2014).
- [43] M. Lemoine and G. Pelletier, *Mon. Not. R. Astron. Soc.* **402**, 321 (2010).
- [44] R. C. Davidson, D. A. Hammer, I. Haber, and C. E. Wagner, *The Physics of Fluids* **15**, 317 (1972).
- [45] A. Achterberg, J. Wiersma, and C. Norman, *Astronomy & Astrophysics* **475**, 19 (2007).
- [46] J. R. Peterson, S. Glenzer, and F. Fiuza, *Phys. Rev. Lett.* **126**, 215101 (2021), arXiv:2104.08246 [physics.plasm-ph].
- [47] J. R. Peterson, S. Glenzer, and F. Fiuza, *Astrophys. J. Lett.* **924**, L12 (2022), arXiv:2201.03547 [astro-ph.HE].
- [48] E. S. Weibel, *Phys. Rev. Lett.* **2**, 83 (1959).
- [49] P. H. Yoon and R. C. Davidson, *Phys. Rev. A* **35**, 2718 (1987).
- [50] J.-i. Sakai, T. Nakayama, Y. Kazimura, and S. Bulanov, *J. Phys. Soc. Jpn.* **69**, 2503 (2000).
- [51] L. O. Silva, R. A. Fonseca, J. W. Tonge, W. B. Mori, and J. M. Dawson, *Phys. Plasmas* **9**, 2458 (2002).
- [52] C. Jaroschek, H. Lesch, and R. Treumann, *Astrophys. J.* **618**, 822 (2005).
- [53] D. Groselj, L. Sironi, and A. Spitkovsky, *Astrophys. J. Lett.* **963**, L44 (2024), arXiv:2401.02392 [astro-ph.HE].
- [54] C. B. Schroeder, C. Benedetti, E. Esarey, F. J. Grüner, and W. P. Leemans, *Phys. Rev. Lett.* **107**, 145002 (2011), arXiv:1108.1564 [physics.plasm-ph].
- [55] M. Reiser, *Theory and design of charged particle beams* (John Wiley & Sons, 2008).
- [56] N. Shukla, J. Vieira, P. Muggli, G. Sarri, R. Fonseca, and L. Silva, *J. Plasma Phys.* **84**, 905840302 (2018).
- [57] S. Ma, *Transverse Emittance Measurements and Optimization for a Superconducting RF Photo Injector*, Ph.D. thesis, Staats- und Universitätsbibliothek Hamburg Carl von Ossietzky (2022).
- [58] T. M. Kneiske, T. Bretz, K. Mannheim, and D. H. Hartmann, *Astron. Astrophys.* **413**, 807 (2004), arXiv:astro-ph/0309141.
- [59] M. Alawashra, I. Vovk, and M. Pohl, (2024), arXiv:2412.01406 [astro-ph.HE].
- [60] J. Buon, CAS CERN Accelerator School 5th General Accelerator Physics Course , 7 (1994).